

The stellar populations in the low luminosity, early-type galaxy NGC59

A. E. Sansom,^{1*} J. J. Thirlwall,¹ M. A. Deakin,¹ P. Väisänen,^{2,3} A. Y. Kniazev,^{2,3,4} and J. Th. van Loon,⁵

¹*Jeremiah Horrocks Institute, University of Central Lancashire, Preston PR1 2HE, UK*

²*South African Astronomical Observatory, P.O. Box 9 Observatory, Cape Town, South Africa*

³*Southern African Large Telescope, P.O. Box 9 Observatory, Cape Town, South Africa*

⁴*Sternberg Astronomical Institute, Lomonosov Moscow State University, Universitetskij Pr. 13, Moscow, 119992, Russia*

⁵*Lennard-Jones Laboratories, Keele University, Staffordshire, ST5 5BG, UK*

30 March 2015

ABSTRACT

Low luminosity galaxies may be the building blocks of more luminous systems. Southern African Large Telescope (SALT) observations of the low luminosity, early-type galaxy NGC59 are obtained and analysed. These data are used to measure the stellar population parameters in the centre and off-centre regions of this galaxy, in order to uncover its likely star formation history. We find evidence of older stars, in addition to young stars in the emission line regions. The metallicity of the stellar population is constrained to be $[Z/H] \sim -1.1$ to -1.6 , which is extremely low, even for this low luminosity galaxy, since it is not classed as a dwarf spheroidal galaxy. The measured $[\alpha/Fe]$ ratio is sub-solar, which indicates an extended star formation history in NGC59. If such objects formed the building blocks of more massive, early-type galaxies, then they must have been gaseous mergers, rather than dry mergers, in order to increase the metals to observed levels in luminous, early-type galaxies.

Key words: galaxies:elliptical and lenticular, cD – galaxies: stellar content – galaxies: abundances – galaxies: individual: NGC59

1 INTRODUCTION

The early-type galaxy NGC59 is similar in morphology to many other low luminosity E or S0 galaxies. It has a stellar mass of $\sim 5 \times 10^8 M_\odot$. This is about 1/200th of M^* (the knee in the overall galaxy mass function for galaxies in the local Universe), taking $\text{Log}(M^*/M_\odot) = 10.64$ from Kelvin et al. (2014). These galaxies form an interesting class of objects whose place in the overall scheme of galaxy evolution has yet to be properly understood.

The hierarchical merger picture of galaxy evolution implies that lower mass galaxies formed before more massive galaxies and that they contributed to the content of more massive galaxies through mergers, over time. Early-type galaxies (ETGs, including elliptical and lenticular) are thought to be particularly affected by this process. Thus, some of the original lower mass galaxies would be consumed in producing giant ellipticals, whilst others, which did not take part in mergers, would still exist today. These ancient relics may look very different today from what they were

like at earlier times. For example, at early times they must have contained gas, with which to make new stars, post-merging. This is because the stellar populations of giant galaxies are not the same as those in lower mass galaxies (e.g. Bender, Burstein & Faber 1993; Worthey 1998). In particular, stars in giant galaxies tend to be more metal-rich than stars in lower mass galaxies. This is the well known mass-metallicity relation, which applies to all types of galaxies (e.g. Gallazzi et al. 2006; Foster et al. 2012). Massive ETGs are also known to have higher $[Mg/Fe]$ ratios than lower mass ETGs (Worthey 1998), or more generally enhanced $[\alpha/Fe]$ element ratios. These are generally interpreted as due to more rapid star formation timescales in massive ETGs, because of the relative timescales of different supernova contributions. However alternative explanations have been suggested for varying $[\alpha/Fe]$ ratio, including systematic variations with galaxy mass of the initial stellar mass function or SNIa delay times, or selective wind mass losses may also affect this ratio (e.g. Pipino et al. 2009).

Lower mass galaxies that survive, without being destroyed in mergers, would continue with their star formation histories (SFHs), unabated. As yet there have not been many

* E-mail: aesansom@uclan.ac.uk

measurements or modelling of abundance patterns from integrated light in ETGs with velocity dispersions below about $\sigma < 80 \text{ km s}^{-1}$. Trends observed at higher velocity dispersions have been well studied (e.g. Pipino et al 2009; Graves, Faber & Schiavon 2009; Conroy et al. 2014), showing hints of increased scatter at lower velocity dispersions. More diverse properties at lower mass might be expected from the greater impact of star forming events on the energetics of systems with smaller gravitational wells (Merlin et al. 2012).

With NTT data we previously investigated a small sample of nearby, low luminosity, early-type galaxies (hereafter LLEs) (Sansom & Northeast 2008). The purpose was to compare their stellar populations and kinematics with their more luminous and more massive counterparts (closer to M^* and above) and with similar mass bulges of spiral galaxies. We found that the LLEs fell below extrapolations of trends in metal line-strengths, but were consistent with spiral bulges of similar velocity dispersion. Fitted luminosity weighted mean ages were found to be young (Ages < 3 Gyr) and abundances covered a wide range ($-1.4 < [\text{Fe}/\text{H}] < +0.1$), with low $[\alpha/\text{Fe}]$ ratios (typically sub-solar). These stellar population characteristics are very different from those of luminous ETGs (e.g. Thomas et al. 2005). The only other galaxies where such characteristics have been detected are in some resolved star data for Local Group dwarf spheroidals (Venn et al. 2004, their fig. 2; Tolstoy et al. 2009), which are much fainter than our original sample of LLEs, and have stellar masses of only a few $\times 10^7 M_\odot$ or less ($< M^*/1000$). The low $[\alpha/\text{Fe}]$ results found for our sample of LLEs have been used to test initial mass functions (IMF) in galaxies, supporting a steeper integrated galactic IMF with increasing galaxy mass and decreasing star formation rate (Recchi, Calura and Kroupa 2009). LLEs provide important tests of scaling relations with mass and luminosity in general, since they are at one extreme of those relations.

A few other studies have measured detailed stellar population parameters in LLEs, including that of Annibali et al. (2011), who studied a small sample of ETGs with M_R in the range -19.8 to -14.8 . They found generally sub-solar metallicities and sub-solar $[\alpha/\text{Fe}]$ on average, with some hints of environmental dependencies, when comparing their ETGs in poor groups with results from the Coma cluster. Koleva et al. (2013) (and references therein) measured stellar population age and $[\text{Fe}/\text{H}]$ in samples of dwarf ETGs and transition-type dwarfs, covering $M_B = -19.0$ to -14.5 and found a wide range of, typically sub-solar metallicities, around -0.7 dex on average, from their luminosity weighted, simple stellar populations (SSP) fits.

The signal-to-noise in LLE spectra is generally not as high as for many luminous ETGs that have been the subject of stellar population analysis. Therefore results for LLEs may be more susceptible to the well known age-metallicity degeneracies that plague such analysis. It is for this reason that we wished to check our results for the most extreme LLEs, using new data that is more sensitive to stellar population parameters. From our NTT data we found that the S0 galaxy NGC59 ($M_B = -15.57$) had central stellar velocity dispersion of $37 \pm 5 \text{ km s}^{-1}$ and the following stellar population parameter estimates: Age $= 1.5 \pm 0.1$ Gyr, $[\text{Fe}/\text{H}] = -1.350 \pm 0.075$ and $[\alpha/\text{Fe}] = -0.300 \pm 0.075$ dex. Whilst other LLEs that we observed also had similarly unusual stellar populations, NGC59 was the most extreme.

Therefore, in this paper we test the results for this galaxy with new data, taken with the SALT telescope (O'Donoghue et al. 2006), covering a wavelength range extending further into the blue region and using stellar population models, based on state-of-the-art stellar spectral libraries.

NGC59 is classified as SA0 in RC3 (de Vaucouleurs et al. 1991) and E in the APM Bright Galaxy Catalogue (Loveday 1996). It is usually classified as a dwarf, early-type galaxy. Bouchard et al. (2005) re-classified this galaxy to a dS0 Pec on the basis of its HI and $\text{H}\alpha$ detections. Beaulieu et al. (2006) measured $\text{HI} = 1.4 \pm 0.1 \times 10^7 M_\odot$ in NGC59 and suggest that this HI mass and $m(\text{HI})/L_B$ ratio are closer to those of dIrr and normal spiral galaxies than dEs. Star formation activity was detected by Skillman, Côté & Miller (2003), in which the $\text{H}\alpha$ image shows lumpy, approximately central $\text{H}\alpha$ emission (their fig. 1). Images in several wavebands are also shown in Saviane et al. (2008, their fig. 1). The nucleus of NGC59 was resolved in J, H and K images, revealing two peaks ≈ 2.3 arcsec apart (de Swardt, Kraan-Korteweg & Jerjen 2010, their fig. 3), with the northern component assumed to be the true stellar nucleus and the southern component a star-forming region. De Swardt et al. (2010) also estimated the total stellar mass of NGC59 to be $5 \pm 2 \times 10^8 M_\odot$, from their H band data. NGC59 is nearby, at a distance of only 4.4 Mpc and it is part of the Sculptor group of galaxies. The proximity and unusual stellar population in NGC59 make it an interesting early-type dwarf galaxy to study. More observations of ETGs in this low mass regime will help to constrain models of galaxy formation.

The observations are described in section 2, then the data reductions are presented in section 3, including kinematics and emission-line strengths. Absorption lines are measured in section 4 and stellar population analysis is presented in section 5. Section 6 gives the conclusions.

2 SALT OBSERVATIONS

SALT is an 11 metre optical telescope that is optimised to be efficient in the blue region of the spectrum, thanks to its optical design and coatings. We used the Robert Stobie Spectrograph (RSS) on SALT to obtain medium resolution spectra across a broad wavelength range (Burgh et al. 2003, Buckley et al. 2008). For the extreme blue part of the spectrum we used the PG3000 grating, covering 3440 to 4220 Å, with slit width 0.6 arcsec, giving a resolution of 1.18 Å (0.26 Å/pix). For redder wavelengths we used the PG1300 grating, covering 3990 to 6080 Å, with slit width 1.25 arcsec, giving a resolution of 2.20 Å (0.67 Å/pix). For both the blue and red spectra the binning was a factor of 2 in the spectral direction and a factor of 4 in the spatial direction, giving 0.5068 arcsec per spatial bin along the slit. The data were observed between 24/05/2012 and 11/10/2012, including 3×800 plus 1100 seconds in the blue and 3×900 seconds in the red, plus observations of three Lick standard stars in both blue and red spectral modes. All observations were performed in seeing conditions between 2 and 3 arcsec. The slit position was along the minor axis of NGC59, at PA $= 37^\circ$ east of north (or 180 degrees around from there), for all spectra except for one of the PG3000 spectra which had PA $= 65^\circ$. These latter data were included to increase the signal-to-noise in the blue. Fig. 1 shows a red DSS image of

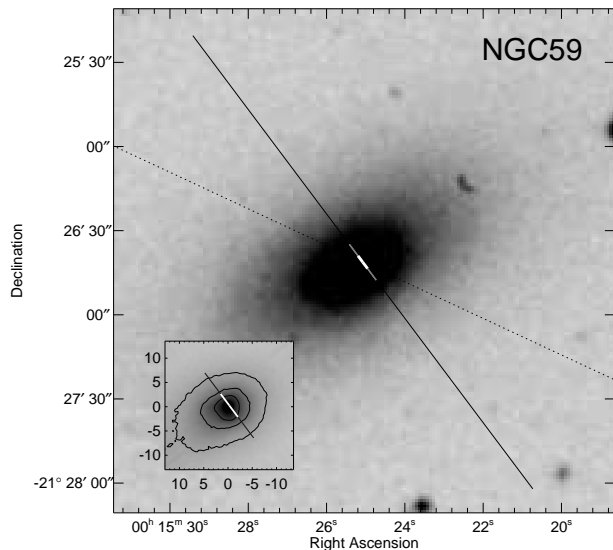


Figure 1. A 3×3 arcmin photographic red DSS image of NGC59, north is up, east to the left. The main RSS slit orientation $PA=37^\circ$ is overlaid on the image with a solid line, and the extracted apertures indicated: the white part of the line is the Central region, and the grey sections of the line indicate the Lower (south west) and Upper (north east) apertures discussed in the text (Section 3.1). The $PA=60^\circ$ slit is shown as the dotted line. The inset shows the nuclear area from the RSS acquisition image with clear filter, where some photometric asymmetry is evident. The inset tick marks are in arcsec.

the galaxy with the slit positions overlaid. The inset is a zoom-in of the nucleus on our short 3 sec RSS acquisition image in white light. In poor seeing conditions a north-south elongation of the nucleus is just detectable, corresponding to the direction of the second nucleus apparent in fig.3 of de Swardt et al. (2010).

The detector consists of three adjacent CCDs with two gaps. We chose wavelength ranges so as to minimize the loss of important regions of the spectra. Thus the blue spectrum covers higher order Balmer lines from $H\delta$ and above, plus the Ca H&K features, whilst the red spectrum covers from $H\delta$ up to the NaD doublet. This then includes most of the standard Lick spectral indices, which are extensively used in stellar population analysis (Worthey et al. 1994, Proctor & Sansom 2002, Johnsson et al. 2013), plus higher order Balmer lines, which are sensitive to the age of the most recent star formation (Worthey & Ottaviani 1997).

3 DATA REDUCTIONS

3.1 Basic Reductions

The preliminary reduced data obtained from the SALT pipeline (Crawford et al. 2010) were further reduced in IRAF. We divided by an illumination flat and wavelength calibrated the spectra, giving a typical uncertainty of ± 0.06 Å in the blue and ± 0.18 Å in the red. At the centres of these two spectral ranges this corresponds to velocity uncertain-

ties of 4.7 and 10.7 km s^{-1} respectively. The 2-d data were cosmic ray cleaned using *xzap* in IRAF and the spectra were background subtracted using a 2nd order polynomial. A relative flux calibration was carried out using flux standard star EG21, from observations taken as close in time as possible to the galaxy observations. This was done with a spline fit, order 6 applied to the flux standard data. The galaxy spectra were then combined using *lscombine*, with additional cosmic ray cleaning, to give two cleaned, summed spectra, one in the blue and one in the red, with a total exposure of 3500 seconds in the blue spectrum and 2700 seconds in the red spectrum for the target galaxy.

A few cosmic ray features remained in the 2-d spectral images, despite efforts to clean them automatically in the processing above. Therefore, we also carried out a final visual check of the spectral images and patched out any remaining cosmic-ray effects that we could identify. This does not preclude the presence of faint cosmic rays, which would go unnoticed against the background of rapidly changing light across the spectral images for NGC59.

Error arrays for the galaxy observations were generated initially from the counts in the original 2-d data files and errors were propagated at each step in the data reductions. The resultant random error arrays highlight where the noise is highest (e.g. due to strong sky lines, emission lines in the galaxy and increasingly towards the blue end of the PG3000 grating spectrum). These arrays were used in the subsequent analysis, including determination of signal-to-noise ratios.

Spectra were extracted for the three Lick calibration stars, which are also velocity standard stars, for the flux calibration stars and for the galaxy observations, in each of the blue and red spectral modes. The spectra for Lick stars and for the galaxy were flux calibrated using the standard star data. This is a relative flux calibration only, since absolute flux calibration is difficult with SALT and weather conditions cannot be assumed to be photometric.

Three spatial regions in NGC59 were measured:

- (i) Central region covers $r_e/8$ either side of centre, which is 11 spatial pixels across (5.6 arcsec), taking r_e as 21.73 arcsec from RC3.
- (ii) Upper region covers 10 spatial pixels above the central region (5.1 arcsec).
- (iii) Lower region covers 10 spatial pixels below the central region (5.1 arcsec).

The central spatial region corresponding to a radial extent of $r_e/8$ (~ 11 pixels in diameter) has a typical signal-to-noise ratio of $S/N \approx 47$ in the blue spectrum and $S/N \approx 60$ in the red spectrum, ignoring the blue regions (below ~ 3800 Å, where the S/N drops rapidly).

3.2 Kinematics and Emission Lines

The Lick standard stars were first analysed in order to align them to a rest wavelength scale. The spectra were cross-correlated to determine their relative spectral shifts. The heliocentric velocity of one template star was found from the SIMBAD database and used to determine observed shifts for all the Lick standard stars. Once these shifts were known *dopcor* and *dispcor* in *iraf* were used to correct and resample the star spectra to a rest wavelength scale, with the same range and sampling as for the galaxy data. The aligned Lick

star spectra could be used as templates for measuring galaxy kinematics, since the stars and galaxy were observed with the same setup. The penalized pixel fitting *pPXF* software (Cappellari and Emsellem 2004) was used to measure kinematics for NGC59, using the PG1300 data only. Emission lines, gap regions, residual sky lines and edges were masked out for these measurements. This gave a first velocity dispersion estimate of $27 \pm 11 \text{ km s}^{-1}$ and a measured recession velocity of $332 \pm 9 \text{ km s}^{-1}$.

Since there were only three Lick standard stars observed, the template match to NGC59 was not very accurate. To improve the accuracy of template stars to describe the absorption line spectrum in NGC59, template spectra of SSPs based on stars in the MILES spectral library from 2006 were used (Sarzi private communication). To use the MILES spectra, the SALT spectra were Gaussian blurred to the same spectral resolution of 2.5 \AA FWHM (Falcón-Barroso et al. 2011). Running the *pPXF* software on these blurred SALT data for NGC59, with the MILES SSPs as templates led to the second velocity dispersion estimate of $47 \pm 23 \text{ km s}^{-1}$.

Both of these estimates are similar to our previous estimate of $37 \pm 5 \text{ km s}^{-1}$, using data from the NTT with a large sample of Lick standard stars (Sansom & Northeast 2008). For the rest of this paper we use this previous estimate of velocity dispersion, since it was obtained using more kinematic standard stars, giving a better template match to the galaxy at the resolution of those observations.

In order to measure emission lines the two SALT gratings (PG3000 and PG1300) were first combined, from the same spatial region as far as possible, in the following way. Both the spectra were resampled onto the full spectral range (3440.6 to 6080.0 \AA) at the binning of the PG1300 spectra, then the overlap region (3990.0 to 4219.8 \AA) was normalised to the PG1300 value, halved, added together with the shorter and longer wavelength data from single grating observations. This led to a spectrum that was well matched across the two grating observations. This spectrum was then blurred to the resolution of MILES, so that the full range of MILES SSP spectra could be used as templates during the emission line measurements. The spectrum of NGC59 was also binned to the MILES sampling of $0.9 \text{ \AA}/\text{pixel}$. A best fit template spectrum (Best_Template), combining several SSPs, was obtained by running *pPXF* with the emission lines masked out. The Best_Template was output as a spectrum, with Galactic extinction incorporated to match the observations, assuming Calzetti et al. (2000) reddening plus Galactic $E(B-V)=0.019 \text{ mag}$, from NED¹.

Emission lines in the spectrum of NGC 59 were then accurately measured, making use of the Best_Template and applying programs described in detail in Kniazev et al. (2004, 2005). Table 1 lists the measured relative intensities of all detected emission lines relative to $H\beta$ ($F(\lambda)/F(H\beta)$) and the ratios corrected for the extinction ($I(\lambda)/I(H\beta)$). The EW of the $H\beta$ emission is also listed as is the derived extinction coefficient $C(H\beta)$. The latter is a sum of the internal extinction in NGC 59 and foreground extinction in the Milky Way. The measured $C(H\beta)$ corresponds to a V-band extinction of $A_V = 0.59 \text{ mag}$. Accounting for the Milky Way foreground extinction of 0.06 mag (Schlegel, Finkbeiner, & Davis 1998) this suggests non-negligible dust content of $A_V \sim 0.5 \text{ mag}$ extinction in the central HII region of NGC 59.

Our emission line measurement programs determine the location of the continuum, perform a robust noise estimation, and fit separate lines by a single Gaussian superimposed on the continuum-subtracted spectrum (Kniazev et al. 2004). In this particular case since a best-fit model was already created, the model was used as the continuum. The quoted errors of single line intensities include components summed up in quadrature (Kniazev et al. 2004). The total errors were propagated in the calculations and are included in the uncertainties of the element abundances and all other derived parameters presented here. Note that our programs are designed to derive simultaneously both the extinction coefficient $C(H\beta)$ and the absorption equivalent width $EW_{abs}(\lambda)$ for the hydrogen lines as described in Izotov, Thuan, & Lipovetsky (1994). We can use this to check the consistency between the model continuum and the emission lines. The result for absorption lines is $EW_{abs}(\lambda)=0.00 \pm 0.13 \text{ \AA}$ which means that the model that was subtracted describes very well the Balmer absorption since no additional component is needed to explain the emission line ratios beyond extinction. We experimented with slightly different models as well, and also by forcing $EW_{abs}(\lambda)=0$, and the results for all emission line parameters stay the same within the uncertainties, which also stay the same. We note that the uncertainty of 0.13 for the Balmer absorption is propagated through all the results, and, in fact, is very similar to the uncertainty of the Balmer line Lick indices derived below by very different and independent methods.

The HII region spectrum was interpreted by the technique of plasma diagnostics and iterative calculations as described in detail in Kniazev et al. (2008). The results regarding temperatures, the number density n_e derived using the $[OII] \lambda 3726/\lambda 3729$ lines ratio, and the total elemental abundances for O, Ne and Cl, are given in Table 2. The electron temperature $T_e(OIII)$ was calculated directly using the weak auroral line of oxygen $[O III] \lambda 4363$.

The relative emission line intensities given in Table. 1 are consistent with a star-forming origin, considering the location of $[OIII]/H\beta$ versus $[OII]/[OIII]$ in the line ratio diagrams like those of Baldwin, Phillips and Terlevich (1981), their figure 2. This is consistent with the findings of previous authors. Skillman, Cote & Miller (2003) mapped and analysed the $H\alpha$ emission in NGC59. From $H\alpha$ emission and GALEX FUV fluxes, Karachentsev & Kaisina 2013 estimated star formation rates of $SFR_{H\alpha}=0.0123 \text{ M}_{\odot} \text{ yr}^{-1}$ and $SFR_{FUV}=0.0063 \text{ M}_{\odot} \text{ yr}^{-1}$ respectively, which agree quite well within their expected uncertainty of ~ 50 per cent, confirming the star forming origin of the emission lines. Bouchard et al. (2005) suggested that NGC59 be reclassified as dS0 Pec, due to the detection of neutral and ionised components near the centre. All the reddening corrected Balmer lines measured here (Table. 1), including the well determined higher order lines ($H9$ to $H11$), show ratios that are consistent with expectations for hydrogen recombination lines from a typical HII region (e.g. Skillman et al. 1994).

Abundances in the gas were estimated from the observed emission lines, using the software of Kniazev, with the direct method because the $[OIII]$ line at 4363 \AA is detected. The oxygen abundance $12+\log(O/H) = 8.13 \pm 0.03 \text{ dex}$ (i.e. $\sim 1/5$ Solar, e.g. compared to Grevesse & Sauval 1998) that we find for NGC 59 is reasonably consistent with

Table 1. Emission line measurements relative to $H\beta$. The relative intensities are measured from NGC 59 after continuum model subtraction, using programs described in Kniazev et al. (2004, 2005). Note that the derived Balmer absorption $EW(abc) \approx 0$ indicates the absorption was correct in the continuum model (see text). Extinction is derived from a simultaneous iterative fit to the emission line intensities, absorption characteristics and temperature information using the direct method with the $[O III] \lambda 4363$ Auroral line. All relevant errors have been propagated to the uncertainties including those from the continuum fitting.

$\lambda_0(\text{\AA})$ Ion	$F(\lambda)/F(H\beta)$ (measured)	$I(\lambda)/I(H\beta)$ (corrected)
3727 [O II]	1.8667 \pm 0.0857	2.2846 \pm 0.1089
3771 H11	0.0140 \pm 0.0040	0.0170 \pm 0.0070
3798 H10	0.0214 \pm 0.0034	0.0259 \pm 0.0065
3835 H9	0.0513 \pm 0.0032	0.0614 \pm 0.0061
3868 [Ne III]	0.4282 \pm 0.0095	0.5094 \pm 0.0125
3889 He I + H8	0.1847 \pm 0.0049	0.2189 \pm 0.0079
3967 [Ne III] + H7	0.2315 \pm 0.0103	0.2702 \pm 0.0133
4026 He I	0.0146 \pm 0.0011	0.0169 \pm 0.0012
4068 [S II]	0.0227 \pm 0.0026	0.0260 \pm 0.0030
4076 [S II]	0.0041 \pm 0.0009	0.0047 \pm 0.0011
4101 H δ	0.2550 \pm 0.0058	0.2902 \pm 0.0083
4340 H γ	0.4220 \pm 0.0094	0.4600 \pm 0.0112
4363 [O III]	0.0492 \pm 0.0017	0.0535 \pm 0.0019
4471 He I	0.0297 \pm 0.0017	0.0317 \pm 0.0018
4861 H β	1.0000 \pm 0.0294	1.0000 \pm 0.0297
4922 He I	0.0081 \pm 0.0011	0.0081 \pm 0.0011
4959 [O III]	1.5665 \pm 0.0335	1.5432 \pm 0.0332
5007 [O III]	4.7950 \pm 0.1026	4.6896 \pm 0.1009
5518 [Cl III]	0.0046 \pm 0.0011	0.0042 \pm 0.0010
5538 [Cl III]	0.0028 \pm 0.0008	0.0025 \pm 0.0007
5876 He I	0.1212 \pm 0.0029	0.1054 \pm 0.0027
C($H\beta$) dex	0.28 \pm 0.04	
E(B-V) mag	0.19 \pm 0.03	
A_V mag	0.59 \pm 0.08	
$EW(abc)$ \AA	0.00 \pm 0.13	
$EW(H\beta)$ \AA	44 \pm 1	

Table 2. Elemental abundances in NGC 59.

$T_e(OIII)(K)$	12,139 \pm 173
$T_e(OII)(K)$	11,952 \pm 149
$N_e(OII)(cm^{-3})$	48 \pm 33
$O^+/H^+(\times 10^5)$	4.477 \pm 0.297
$O^{++}/H^+(\times 10^5)$	9.161 \pm 0.418
$O/H(\times 10^5)$	13.640 \pm 0.513
$12+\log(O/H)$	8.13 \pm 0.03
$Ne^{++}/H^+(\times 10^5)$	2.678 \pm 0.149
ICF(Ne)	1.141
$Ne/H(\times 10^5)$	3.06 \pm 0.17
$12+\log(Ne/H)$	7.49 \pm 0.02
$\log(Ne/O)$	-0.65 \pm 0.03
$Cl^{++}/H^+(\times 10^7)$	0.291 \pm 0.056
ICF(Cl)	1.286
$Cl/H(\times 10^7)$	0.37 \pm 0.07
$12+\log(Cl/H)$	4.57 \pm 0.08
$\log(Cl/O)$	-3.56 \pm 0.08

the abundance 8.29 ± 0.08 dex published by Saviane et al. (2008). Our data also allow us, for the first time, to determine abundances of Ne and Cl in NGC 59, which are also approximately 1/5 Solar to within about 20%. It is known that HII region abundances mainly provide information about α -process elements, which are produced predominantly in short-lived massive stars. The relative abundances of $\log(Ne/O)$ and $\log(Cl/O)$ in Table. 1 are consistent with values for a large sample of HII regions in blue compact galaxies Izotov & Thuan (1999) and a large sample of HII galaxies (Izotov et al. 2006) from the Sloan Digital Sky Survey DR3 data (Abazajian et al. 2005).

3.3 Removing Emission Lines

Subtracting the emission lines proved difficult to do accurately, since emission lines near the centre of NGC59 are quite strong and their spectral shape in the SALT data did not appear to follow a Gaussian accurately enough to subtract them well using *gandalf* (Sarzi et al. 2006). An alternative solution was used to remove the estimated contributions from emission lines. For all hydrogen Balmer lines in the spectral range, core regions (width ~ 10 \AA) affected by emission were replaced by data from Best_Template, as our best estimate of the shape and strength of the hydrogen absorption line cores. This is illustrated in Fig. 2, which shows a closeup of the Balmer line regions, illustrating the original data (thick cyan line), the best fit template (thick dark blue line) and the data with Balmer cores replaced (thin black line). For other emission lines, simple interpolation across the lines was applied and these regions flagged for subsequent information. Fig. 3 shows the original central spectrum (top plot), then the final central spectrum with the hydrogen line emission replaced and other emission lines removed (lower plot). Although we are replacing part of the hydrogen lines by template data, rather than real data for NGC59, this produces more realistic hydrogen absorption line shapes than subtracting the emission lines using *gandalf*. This replacement process was thought to be the best compromise, given that the core absorption line data is lost due to the strong emission lines. H7 at 3970 \AA is lost in one of the gaps, but many other Balmer lines are clearly visible. The consistency of measured higher order Balmer line emissions (shown in Table. 1) helps to support the validity of our approach. Higher order Balmer absorption lines are less affected by emission line contamination.

At short wavelengths there is a hint of UV upturn in the spectrum (Kaviraj et al. 2007), however near the blue edge of the data, below ~ 3500 \AA the flux calibration becomes unreliable.

4 ABSORPTION LINE MEASUREMENTS

Standard Lick absorption lines were measured using the *Lector* software available from <http://miles.iac.es/pages/software.php>. Perturbations applying the error arrays were used to generate 500

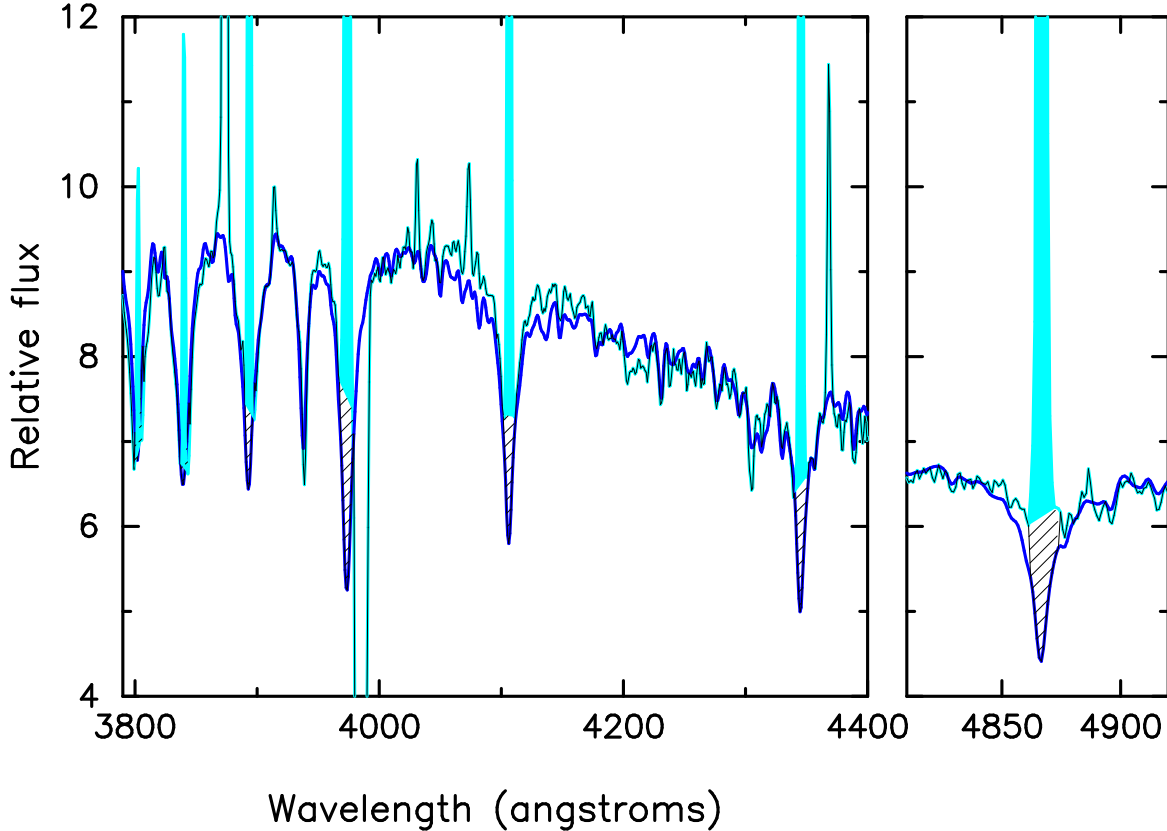


Figure 2. Balmer line regions in the central spectrum in NGC59, illustrating the replacement of the cores of Balmer lines, where strong emission lines originally dominated those data. The thick cyan lines are the original spectral data, the thick dark blue lines are the best fitting MILES template data and the thin black lines are the Balmer line core corrected spectral data. Other emission lines are subsequently removed by interpolation across them, to produce the lower spectrum shown in Fig. 3.

Monte Carlo realisations of the data, from which random errors were estimated for the line-strength measurements. Line-strength errors due to uncertainties in kinematics (velocity and velocity dispersion) were evaluated by varying the assumed kinematic within their estimated errors and re-measuring the line strengths. These uncertainties were found to be significantly less than the random errors. Uncertainties in the Balmer line cores were estimated by trying fits using different parts of the spectrum, but still including all the Balmer lines, including removing the continuum regions above $H\beta$ and below the Balmer limit. This led to estimated Balmer line errors from our core H line replacement procedure. All these errors were added together in quadrature to give total estimated errors for each index. Two Lick features were lost due to partially falling within gap regions (C_24668 and $Fe5406$). Another Lick feature was lost due to falling too close to strong emission lines ($Fe5015$). The data and error estimates are given in Table. 3, for the three regions measured in NGC59.

Fig. 4 shows a plot of these three regions. Evidence of young stars is present in all three spectra, from the strength of the Balmer absorption lines. From the cleaned spectra in Figs. 3 and 4 it is already possible to see that this is a low metallicity galaxy, from the weakness of the metal sensitive lines around Mgb. One possibility to consider for NGC59 is that nebular continuum emission may decrease

its apparent absorption line strengths. Reines et al. (2010) studied relative contributions to continuum emission from stars and gas in young massive star clusters. For example, their figure 8 shows that if all the stars had formed only 5 Myr ago then the nebular continuum is only 5 per cent of the total continuum. The results presented here (e.g. Fig. 3), including strong Balmer absorption lines in NGC59, show that stars older than 5 Myr dominate the light. This is also supported by full spectrum fitting described below in Section 5.4. Therefore the effect of nebular continuum emission is unlikely to cause a significant bias for the Lick absorption line measurements in NGC59.

The upper, off-centre region extends beyond the two peaks of near infrared emission mapped by de Swardt et al. (2010), which they assumed to be associated with the centre of the galaxy and a star-forming peak 2.3 arcsec to the south. Therefore it is interesting to see if different stellar population characteristics are uncovered in these regions beyond the central star-forming area, perhaps better characterising the bulk of stars in NGC59.

Table. 3 shows how the spectra change between central and off-centre regions, with hydrogen absorption lines becoming generally weaker in the lower region. There is an anomalously weak measurement of $Fe5270$ in the lower region, which is investigated below. These data are used to characterise the stellar populations in the next section.

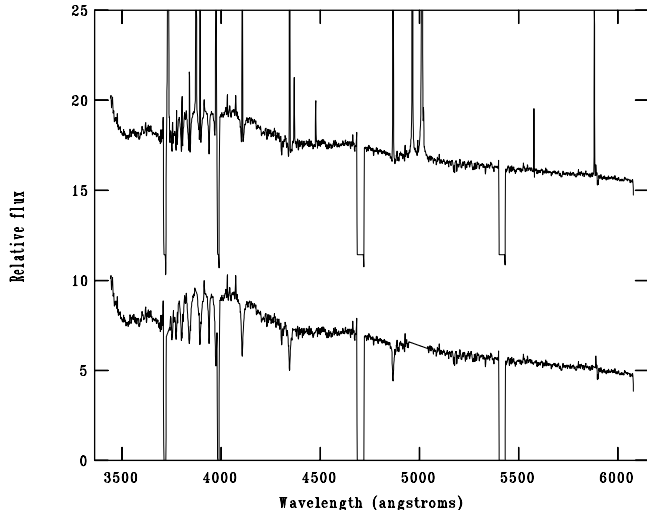


Figure 3. Central spectrum in NGC59. This plot shows the processing to remove emission lines from the spectrum. Data were taken with the SALT telescope in two grating settings, combined as described in the text. The **top plot** is offset vertically and shows the combined data before attempting to remove any emission line features. This shows four gap regions, two associated with each grating observation, centred around 3716 Å and 3985 Å in the blue, and around 4703 Å and 5417 Å in the red. Emission lines are strong and the hydrogen Balmer series shows both emission lines and broader absorption line components. Residual sky line features are apparent at 5577 Å and residual contamination due to strong cosmic rays affects the NaD doublet such that we do not use it in our subsequent analysis in section 5. The **lower plot** shows the same spectrum with the Balmer emission line regions replaced by data from the best fit MILES SSP template and several strong emission lines removed by interpolating across those regions.

5 STELLAR POPULATION ANALYSIS

5.1 Lick System - MILES SSPs

The indices from Table. 3, at the standard Lick resolutions (Worthey & Ottaviani 1997), were used to estimate luminosity weighted average SSP age, metallicity and $[\alpha/\text{Fe}]$ across NGC59. This uses software written by R. Proctor, based on the SSP results of Korn et al. 2005, plus references therein. CN1 was excluded from these fits since it is too strongly affected by H δ in its blue side band. Results are given in Table. 4.

The fit for the lower region led to an old age, qualitatively inconsistent with the presence of emission lines in this spectrum, suggesting some more recent or ongoing star formation. The initial fit was quite poor due to an anomalously low value of Fe5270, which when removed led to a significant improvement in chi-squared at similar parameters. On further inspection, a small peak in the lower spectrum, in the central band of Fe5270 adversely affects this measurement and appears to correspond to a possible weak cosmic ray event in one of the original images. We note that removing a remaining outlier, the Mg1 index, leads to a younger estimated age ($\text{Log}(\text{Age})=0.8$ dex) while the metallicity remains low and the abundance ratio sub-solar. This gives an indi-

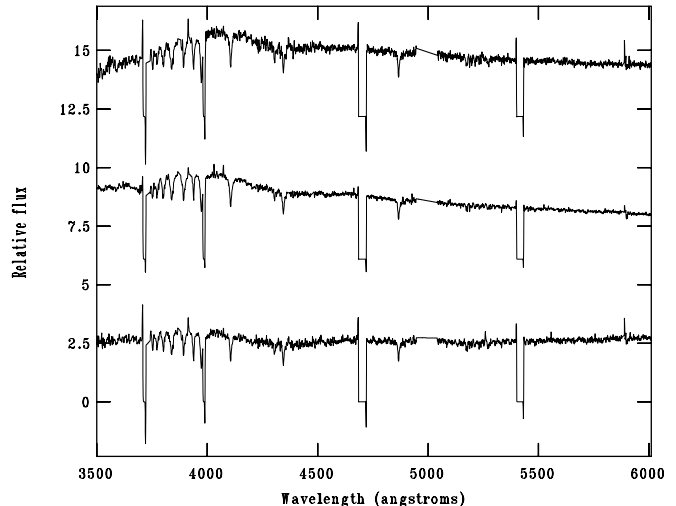


Figure 4. From bottom to top, this plot shows cleaned spectra of the lower, central and upper regions in NGC59, with vertical offsets to separate the plots. The central region is the same as in the lowest plot in Fig. 3. All three spectra have had the cores of their hydrogen Balmer lines replaced by the best fitting SSP template from the MILES SSP database, in order to remove the emission line contamination from those lines. Other strong emission lines have been removed by interpolating across them.

cation of the parameter uncertainties due to the inclusion or exclusion of specific indices. The fit with Fe5270 removed is shown in Table. 4. For this low metallicity ($[\text{Z}/\text{H}] \sim -1.6$) the SSP line-strengths change little with age, for ages greater than 8 Gyrs (see Fig. 5) and the Balmer line-strengths start to vary non-monotonically. Therefore the best fitting SSP age of this lower region is difficult to constrain beyond saying that it is older than ~ 8 Gyrs. The uncertainty in age estimate given for this lower region in Table. 4 is an underestimate since we can only give this lower limit to the age. Therefore we do find evidence of older stars (> 8 Gyr) in NGC59, beyond the central, strongest emission-line region. Jerjen, Binggeli & Freeman (2000) studied its optical brightness profile and colours and found a Sersic index of $n=0.63$ in B, with B-R colour becoming redder further out, indicative of older stars.

The centre region was not well fit by a single SSP ($\chi_r^2 = 2.63$). Outlying indices were removed to see what effect this would have on the fit and derived parameters. Removing 2 indices (Mg1 and Fe5270) brought the χ_r^2 down to 1.4, but did not significantly alter the derived parameter values. Therefore we show the fit including those three indices in Table. 4. In Section 5.3 below we make a preliminary search to see if two SSPs will better describe this central region of NGC59. The metallicity of the centre region is similar to that in the lower region. The low $[\text{Fe}/\text{H}]$ abundance found in the centre of NGC59 is also supported by the Rose indices measured using *Lector* in this region. For NGC59 we measured $\text{H}\delta/\text{FeI}\lambda 4045=0.654$ and $\text{FeI}\lambda 4045/\text{FeI}\lambda 4063=1.012$, which implies $[\text{Fe}/\text{H}] \sim -1.5$ (Rose et al. 1994, their fig. 10). The centre regions has a fitted SSP age of ~ 5 Gyr.

Table 3. NGC59 line strengths measured at **MILES resolution** (FWHM=2.5 Å), for standard Lick band definitions. Standard deviations (SD) are 1 sigma random errors derived from 500 realisations of the spectra, perturbed by the error array. Dsig errors are derived by accounting for the uncertainty in velocity dispersion estimated from the current data. Similarly, Dvel errors are derived by measuring the changes in indices considering the uncertainty in recession velocity. H errors are estimated uncertainties in the Balmer line core replacement. Total errors add all these error sources together, in quadrature. The errors are dominated by the random errors and by Balmer line core uncertainties. The mask values are '1' for good indices, included in later fits, and '0' for indices with problems, excluded from later fits. These latter indices include: C₂4668 and Fe5406, which fall into the gap regions between CCDs; Fe5015, which overlaps regions containing strong emission lines. The line strengths for these three indices are not shown here. This mask array applies to all three spatial regions, unless otherwise stated in the text. Also tabulated are results for the same three regions, at the **Lick standard resolution** (from Worthey & Ottaviani 1997) at FWHM ~8.4 - 10.9 Å.

Name:	H δ_A	H δ_F	CN1	CN2	Ca4227	G4300	H γ_A	H γ_F	Fe4383	Ca4455	Fe4531	H β	Mg1	Mg2	Mgb	Fe5270	Fe5335	Fe5709	Fe5782
Central (r_e/8) region. MILES resolution.																			
Value:	4.856	3.977	-0.098	-0.051	0.176	0.475	3.254	3.132	0.578	0.395	1.286	3.103	0.020	0.041	0.962	0.657	0.688	0.473	0.287
SD err:	0.163	0.116	0.005	0.006	0.092	0.168	0.176	0.124	0.261	0.121	0.180	0.170	0.003	0.003	0.126	0.144	0.153	0.103	0.102
Dsig err:	0.003	-0.003	0.000	0.000	-0.001	0.000	-0.002	-0.014	-0.052	0.016	-0.006	0.003	-0.001	-0.001	-0.007	-0.003	-0.008	-0.001	0.005
Dvel err:	0.000	0.003	0.000	-0.001	0.005	-0.026	0.001	0.002	-0.003	-0.008	-0.005	-0.000	0.000	-0.000	0.009	-0.007	-0.016	0.003	-0.004
H err:	0.638	0.643					0.428	0.428				0.499							
Total err:	0.658	0.653	0.005	0.006	0.092	0.170	0.463	0.446	0.266	0.122	0.180	0.527	0.003	0.003	0.126	0.145	0.154	0.103	0.102
Mask:	1	1	0	1	1	1	1	1	1	1	1	1	1	1	1	1	1	1	1
Upper region. MILES resolution.																			
Value:	4.636	4.013	-0.124	-0.081	0.948	1.469	2.601	3.458	2.468	0.226	1.445	3.488	0.025	0.074	1.227	1.890	1.282	0.483	0.391
Total err:	0.761	0.735	0.010	0.012	0.185	0.357	0.463	0.553	0.507	0.233	0.378	0.484	0.005	0.006	0.241	0.274	0.297	0.187	0.193
Lower region. MILES resolution.																			
Value:	4.143	3.527	-0.077	-0.026	0.434	1.162	2.344	3.167	1.850	-0.212	1.439	2.436	0.032	0.063	0.919	0.457	0.732	0.638	0.177
Total err:	0.719	0.684	0.010	0.012	0.173	0.329	0.375	0.656	0.441	0.232	0.346	0.408	0.005	0.005	0.196	0.228	0.251	0.141	0.141
Central (r_e/8) region. Lick Standard resolution.																			
Value:	4.815	3.644	-0.097	-0.065	0.084	0.290	3.194	2.899	0.468	0.267	1.088	2.996	0.020	0.041	0.830	0.558	0.568	0.435	0.274
Total err:	0.658	0.653	0.005	0.006	0.095	0.171	0.463	0.443	0.277	0.124	0.200	0.526	0.003	0.003	0.127	0.139	0.158	0.103	0.100
Upper region. Lick Standard resolution.																			
Value:	4.670	3.636	-0.127	-0.099	0.667	1.128	2.617	3.215	2.298	0.056	1.369	3.409	0.025	0.073	1.029	1.747	1.057	0.484	0.297
Total err:	0.713	0.736	0.010	0.012	0.191	0.350	0.455	0.549	0.490	0.236	0.396	0.481	0.006	0.006	0.242	0.241	0.301	0.201	0.179
Lower region. Lick Standard resolution.																			
Value:	4.163	3.210	-0.079	-0.044	0.261	0.926	2.275	2.911	1.669	-0.168	1.246	2.493	0.031	0.062	0.871	0.371	0.610	0.516	0.187
Total err:	0.723	0.685	0.010	0.012	0.178	0.333	0.360	0.650	0.479	0.228	0.357	0.411	0.004	0.005	0.186	0.219	0.235	0.139	0.137

The upper region is adequately fit by a single SSP ($\chi^2_r = 1.4$), which is relatively young (3.5 Gyr). The upper region is fit by the highest overall metallicity ($[Z/H] \sim -1.05$), which is still low amongst ETGs. The best fit $[\alpha/Fe]$ ratio is sub-solar in all regions, similar to what we found previously with the NTT data (Sansom & Northeast 2008), where only one spectrum was analysed.

In general the ages and abundance ratios are not very well constrained by these data. However, the very low metallicity in NGC59 ($[Z/H] < 1/10$ th of solar) is a more robust result. These results are illustrated in the index-index plots of specific features shown in Fig. 5, where the locations and uncertainties of the three regions in NGC59 are plotted against grids of MILES SSP predictions.

5.2 Lick System - EZ_Ages

The above results were tested using an alternative stellar library and fitting software called EZ_Ages (Graves & Schiavon 2008), downloaded from http://astro.berkeley.edu/~graves/ez_ages.html. This code uses SSPs based on the Jones and INDO-US stellar libraries, as described in Schiavon (2007) and fits to Lick standard indices. Briefly, at solar abundance pattern, the ages searched are: 1.2, 1.5, 2.5, 2.8, 3.5, 5.0, 7.0, 10.0, and 14.1 Gyrs, and the $[Fe/H]$ values searched are: -1.3 , -0.7 , -0.4 , 0.0 and $+0.2$ dex. EZ_Ages could not be used to fit indices for NGC59 in the central and lower regions because this galaxy has a very low metallicity, falling below the lowest predictions, at $[Fe/H] = -1.3$, in EZ_Ages. This is illustrated in the output index-index plots, an example of which is shown in Fig. 6. Lines of constant $[Fe/H]$ (solid lines) are shown, with $[Fe/H]$ increasing from left to right; plus lines of constant age (dotted lines) have ages increasing from top to bottom in these grid plots. Therefore this figure indicates that the ages in NGC59 are consistent with ~ 2 to 6 Gyrs, based on $H\beta$ as the main age indicator and slightly extrapolating to the left of the plotted grid (i.e. to lower $[Fe/H]$) for the centre and lower regions. For the upper region, which could be fitted with the EZ_Ages software, the following measurements were found: $Age = 2.12^{+1.09}_{-0.45}$ Gyr; $[Fe/H] = -0.80^{+0.26}_{-0.24}$ dex; $[Mg/Fe] = -0.04^{+0.12}_{-0.09}$ dex.

Results for ages and $[Fe/H]$ from the MILES SSP fits are qualitatively consistent with those from EZ_Ages. For the upper region the results from EZ_Ages are also quantitatively consistent within the estimated errors given in Table. 4. One exception is that the best fit age from MILES fits to the lower region is very old. However, recall that we can only place a limit on this age as approximately > 8 Gyrs, as discussed in Section 5.1 above. The good agreement between results from MILES SSP fits and EZ_Ages fits indicates that our SSP fitting results are not biased by the models used to fit the Lick indices.

5.3 New MILES database - Two burst models

We know that galaxies are not SSPs in reality, and that NGC59 shows evidence of very recent star formation in the form of strong emission lines. Here we generate some predictions for two-burst SFHs, using the webtools and the latest version of SSPs from the MILES website (Vazdekis et al.

2010), at the MILES resolution (FWHM=2.5 Å). Composite spectra and Lick indices can be generated and downloaded.

We attempt a search of parameter space to see if the current data for NGC59 are consistent with an old (~ 14 Gyr), metal-poor ($[Z/H] \sim -1.7$) burst plus a younger burst, whose age, metallicity and mass contribution we vary on a grid of models. Younger burst ages are from 0.063 to 1.0 Gyrs, with possible metallicities of $[Z/H] = -1.7, -1.3, -0.7, -0.4, 0.0$ and mass contribution varied from 50 per cent to 0.5 per cent. The rest of the mass is in the old SSP. These combinations were tested against the data for the centre region in NGC59. The best fits are restricted by the fact that no interpolation of SSP models was available from the MILES web site. A similar fit to that shown in Table. 4 could be achieved, but only with the lowest metallicity ($[Z/H] = -1.7$), and a small mass contribution (~ 1.5 per cent) from a young population (0.07 Gyr). This is equivalent to a frosting of young stars on an otherwise old, metal-poor stellar population. The fit became worse if a higher metallicity ($[Z/H] = -0.7$) was assumed for the old or young population. Therefore only fits with low metallicity were possible, supporting the results from single SSP fitting that NGC59 is a very low metallicity galaxy.

Attempting to fit more complex SFH, with intermediate age populations led to poorer fits, since intermediate age populations cannot reproduce weak enough metal sensitive lines, at a given Balmer line-strengths.

5.4 STARLIGHT full spectrum fits

Finally, as an additional check on the analysis, both for Balmer line processing and to check model fits, full spectrum fitting was attempted using STARLIGHT (Cid Fernandes et al. 2005). This was run with Bruzual & Charlot (2003) SSPs, for all the three apertures and with and without the cores of the strongest Balmer lines for each. Whether the Balmer lines were masked out or not, the results are very similar illustrating that our main results are not biased by the Balmer emission line replacement process described in Section 3.3.

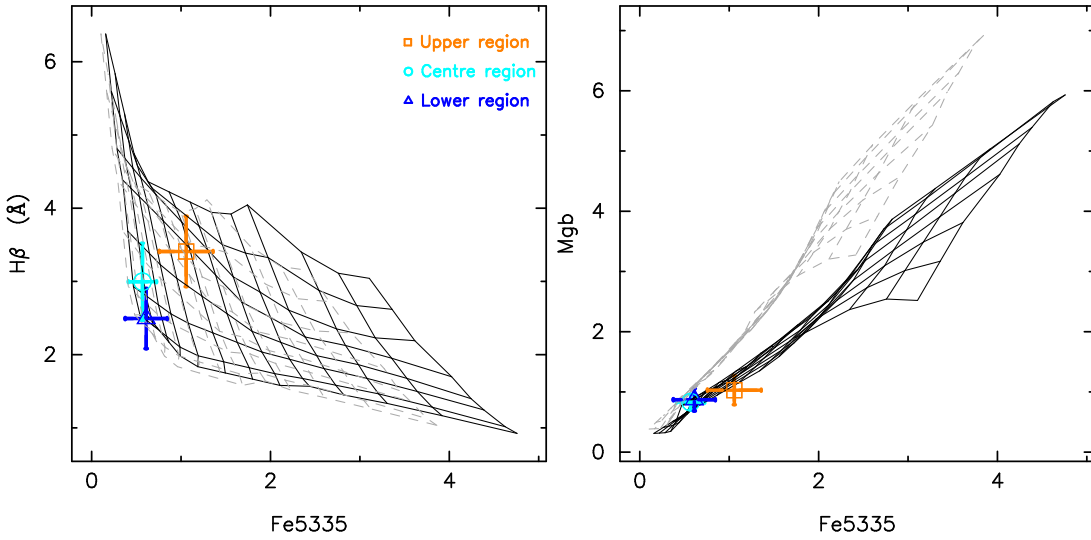
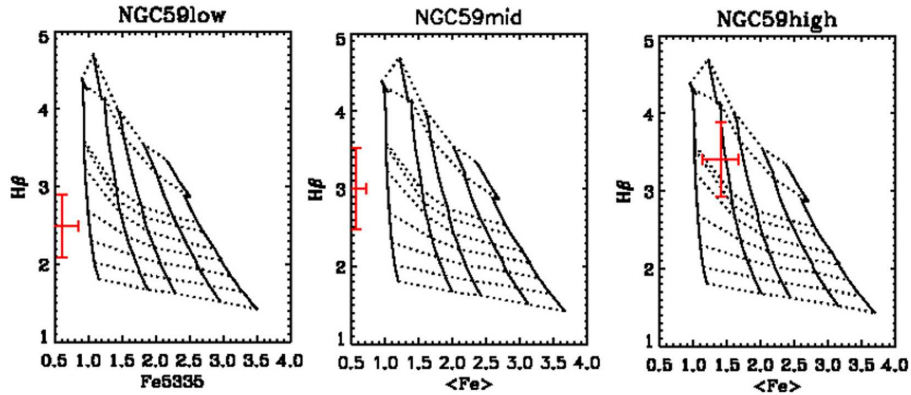
Also the STARLIGHT fits are broadly consistent with the results from fitting Lick indices. The mean light-weighted age is ~ 3 to 4 Gyr in all three spectra. The STARLIGHT results show a wide spread in the Gyr-scale population ages, with quite well-defined very young 5-20 Myr populations in addition which tend to dominate the *light* except in the upper aperture. The STARLIGHT fits indicate that less than 15% of the light could come from populations younger than 25 Myr. Stellar mass is strongly dominated by the old population in all cases, with the oldest population in the lowest aperture similar to the Lick index results. Fitted mean metallicities are generally well below solar ($\sim 1/10$ th of solar) for both young and old populations, except for a young component contributing to the lower spectrum, which is closer to solar. With the input models used with STARLIGHT we are not able to constrain abundance ratios in any way.

5.5 Discussion

The results illustrated in Fig. 5 do not change significantly when other indices combinations are selected, such as the

Table 4. SSP fits from MILES SSP templates at the Lick standard resolution. Note that $[\text{Fe}/\text{H}]$ is estimated from $[\text{Z}/\text{H}]$ and $[\alpha/\text{Fe}]$.

Region	Log(Age) (Gyr) (\pm)	$[\text{Fe}/\text{H}]$ (\pm)	$[\alpha/\text{Fe}]$ (\pm)	$[\text{Z}/\text{H}]$ (\pm)	No. ind.	Chi-sq reduced	Comment
Upper	0.550 0.118	-0.767 0.135	-0.300 0.054	-1.050 0.120	18	23.43	Emission line region
Centre	0.700 0.047	-1.412 0.211	-0.120 0.177	-1.525 0.089	18	44.63	Stronger emission line region
Lower	1.175 0.082	-1.405 0.236	-0.180 0.192	-1.575 0.122	17	26.64	Emission line region; Fe5270 excluded

**Figure 5.** Index results for NGC59, plotted against grids from MILES SSPs. The black grid is for $[\alpha/\text{Fe}]=0$, while the grey grid is for $[\alpha/\text{Fe}]=+0.3$. In the **left plot**, the age indicator $\text{H}\beta$ is plotted, with age increasing downwards on the grid, for $\text{Log}(\text{Age}(\text{Gyr}))=0.0, 0.15, 0.3, 0.475, 0.7, 0.9, 1.075, 1.175$. The metallicity indicator Fe5335 is plotted, with metallicity increasing from left to right, from $[\text{Z}/\text{H}] = -2.25$ to $+0.80$, in steps of 0.25 dex. Solar metallicity is the fourth line from the right. This plot of age versus metallicity sensitive features, shows the low metallicity and relatively young age in NGC59, with the upper region (orange) being the youngest and the lower region being the oldest (dark blue). The centre of NGC59 (cyan) is intermediate in age between the two outer regions. The **right plot**, of Fe5335 versus Mgb , highlights the un-enhanced $[\alpha/\text{Fe}]$ ratios in NGC59.**Figure 6.** Grid plot showing results for NGC59 from EZ_Ages fitting routine, for the three spatial regions across NGC59. The Lick resolution data and errors are shown by the red plus sign. The upper region in NGC59 (right plot) can be fit, with a metallicity lying within the range allowed by EZ_Ages. The lower and centre regions in NGC59 (left and middle plots) cannot be fit, because of the low metal line strengths, indicating metallicities below those allowed for in EZ_Ages (i.e. $[\text{Fe}/\text{H}] < -1.3$). The age indicator ($\text{H}\beta$) is plotted on the vertical axes, whilst metallicity indicators are plotted on the horizontal axes ($\langle\text{Fe}\rangle = \text{Fe5270} + \text{Fe5335}$ or Fe5335).

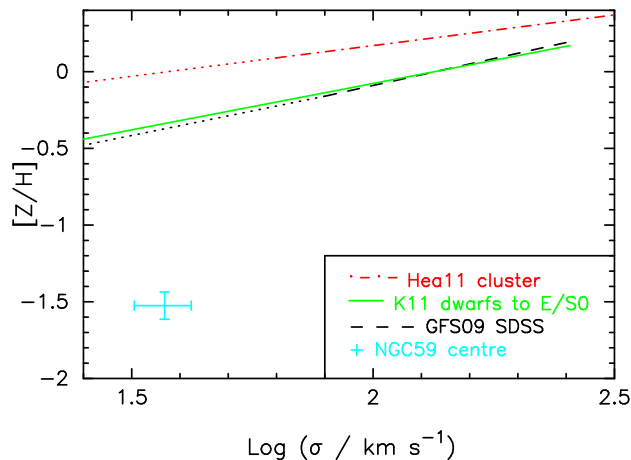


Figure 7. Plot showing $[Z/H]$ relation with $\text{Log}(\sigma)$, for samples of luminous early-type galaxies, compared with results from the current observations for NGC59. The mean trend from Graves et al. (2009) (GFS09) is shown in black and from Harrison et al. (2011) (Hea11) in red, with the current results for NGC59 highlighted by a cyan cross. The trend shown from Koleva et al (2011) in light green uses $[\text{Fe}/H]$ as a proxy for metallicity and includes both dwarf and giant ETGs. Solid lines show the range of $\text{Log}(\sigma)$ covered by the references and extrapolations to lower $\text{Log}(\sigma)$ are shown by dotted lines.

higher order Balmer lines for ages, or the classic $[\text{Mg}/\text{Fe}]$ combination used by many authors as an overall metallicity indicator. The left plot in Fig. 5 illustrates why it is difficult to constrain ages in such low metallicity systems as NGC59, since the grid of models turns up to higher Balmer line strengths, for a given age. This is less apparent in the grid of models plotted in Fig. 6, since those models do not go down to such low metallicities. The right panel in Fig. 5 illustrates the difficulty in measuring $[\alpha/\text{Fe}]$ accurately in such low metallicity systems, since the grids of SSP model predictions start to converge. This indicates how new measures of age and abundance patterns are needed in future, in order to understand the stellar population histories in these potential building block of luminous ETGs. There may be additional information in the bluer part of the spectrum, which is sensitive to abundance patterns (Sansom et al. 2013).

If low mass ETGs formed the building blocks of higher mass ETGs through dissipationless mergers then we might expect to see some relics of those building blocks still around today. They are predicted to have the high metallicity, high $[\alpha/\text{Fe}]$ ratios seen in luminous ETGs, if the build-up of galaxy mass is dissipationless. As yet no such low mass systems have been observed. The quasi-monolithic or early-hierarchical formation of ETGs easily accounts for enhanced $[\alpha/\text{Fe}]$ ratios in more massive galaxies, since there was not time for Fe enrichment from delayed SNIa to feed back into the stellar population. However, simultaneously generating the higher metallicities in such a scenario is difficult (e.g. Pipino et al. 2009, their fig. 8; Merlin et al. 2012, their fig. 13). In fact NGC59 has unusually low metallicity for its mass, making it an unlikely candidate for a dissipationless building block.

A mass-metallicity plot is shown in Fig. 7, with stellar velocity dispersion used as a proxy for mass, in which NGC59 is contrasted with extrapolations from higher σ sys-

tems. The metallicity measured here for NGC59 is well below such extrapolations. These data for NGC59 also fall well below the $[\text{Fe}/H]$ central measurements for dE/dS0 galaxy in the sample of Koleva et al. (2011), their fig. 13, at similar σ , with NGC59 being near the low end of their σ range. Koleva et al. (2011) found a range of, mostly negative, metallicity gradients in their dE/dS0 galaxies.

The above discussion is for metallicities of the stellar populations. The gas metallicity measured in NGC59 is higher, typical of star-forming dwarf galaxies of this mass, as shown in Section 3.2. Systematic uncertainties in the emission line strengths arising from uncertainties in the best fit stellar template were found to be negligible. Metallicities in HII gas associated with recent star formation will be higher than stellar abundances if the latest star formation is most metal enriched in a galaxy. However the estimated gas metallicity in NGC59 is significantly higher than the stellar metallicity. This may indicate that some or all of the gas was accreted from an enriched external source. Alternatively, simulations are needed to explore possible relationships between gas and star metallicities, for different star formation histories, to see how different the gas and star metallicities can become.

More observations of statistically complete samples of lower mass ETGs are needed to probe their ranges of stellar population parameters and how the scaling relations behave at low masses. Such data will provide strong tests for hierarchical merger models of galaxy evolution (e.g. Kaviraj et al. 2009). Future large telescopes, such as the E-ELT, will be able to resolve stellar populations in galaxies at the distance of the Sculptor group, which will allow both an independent check on their stellar metallicities and measurements of their stellar metallicity distributions.

6 CONCLUSIONS

Scaling relations for ETGs rely on accurate data down to low luminosities (e.g. the fundamental plane, or the mass-metallicity relation discussed above). In this paper we looked at one such low luminosity ETG with data from the SALT telescope, covering a broad wavelength range. The data stretch further into the blue region of the spectrum than most previous such studies, allowing for potentially stronger constraints on parameters such as stellar population age and abundance pattern (e.g. see Conroy, Graves & van Dokkum 2014). We also looked across the centre of the system to see how the bulk of the stellar population behaves.

Our main findings are that the low luminosity ETG, NGC59, has a young (SSP age ~ 2 to 6 Gyr), metal poor (SSP $[\text{Fe}/H] \sim -1.4$ to -0.8) population near its centre, with evidence of an older underlying population ($> \sim 8$ Gyr) which is also very metal-poor. The $[\alpha/\text{Fe}]$ ratio is difficult to accurately constrain with these data, for such a low metallicity galaxy, however, all measurements are consistent with slightly sub-solar values. Using two different sets of models led to similar results for the SSP parameters estimated from Lick line strengths. These results are qualitatively in agreement with our previous results for NGC59, but the measured metallicity is even lower than previously estimated. These data highlight the difficulty of measuring accurate ages for metal-poor systems, older than about 8 Gyrs.

Fitting two-burst SSP models gave a better representation of the overall spectrum and NGC59 was best fit with an old (14 Gyr), metal-poor SSP plus a 1.5 per cent mass frosting of young (0.07 Gyr), metal-poor stars. Fits using STARLIGHT led to qualitatively similar results, confirming the low stellar metallicity in NGC59, although no abundance pattern constraints are yet possible with these full spectrum fitting methods. We note that the gas phase metallicity in the HII region close to the nucleus of NGC59 is higher, $[O/H] \sim -0.7$, possibly suggesting external gas accretion of unknown origin. Results such as the ones shown here for NGC59 and for larger samples of LLEs will be useful in future to constrain cosmological simulations and test hierarchical merging models of galaxy evolution and morphological transformations.

ACKNOWLEDGMENTS

All of the observations reported in this paper were obtained with the Southern African Large Telescope (SALT). The proposal code was 2012-1-UKSC-003, and the PI was Sansom. Thanks go to the SALT support scientists for their help with these observations. PV and AYK acknowledge support from the National Research Foundation of South Africa. An RAS grant was awarded for an internship student, M.A.Deakin, to work on these data, plus a UCLan internship for J.J. Thirlwall. Thanks to R. Proctor for the use of his SSP fitting software and to M. Sarzi for help with *pPXF* and *gandalf* software. We thank V.P. Debattista and the anonymous referee for helpful comments that improved the paper.

REFERENCES

- Abazajian, K., et al. 2005, *AJ*, 129, 1755
- Annabali F., Grutzbauch R., Rampazzo R., Bressan A., Zeilinger W.W., 2011, *A&A*, 528, A19
- Baldwin J.A., Phillips M.M., Terlevich R., 1981, *PASP*, 93, 5
- Bender R., Burstein D., Faber S.M., 1993, *ApJ*, 411, 153
- Bouchard A., Jerjen H., Da Costa G.S., Ott J., 2005, *AJ*, 130, 2058
- Bruzual G., Charlot S., 2003, *MNRAS*, 344, 1000
- Buckley D. et al. 2008, *SPIE*, 7014, 6
- Burgh E.B. et al. 2003, *SPIE*, 4841, 1463
- Calzetti D., et al., 2000, *ApJ*, 533, 682
- Cappellari M., Emsellem E., 2004, *PASP*, 116, 138
- Cid Fernandes R., Mateus A., Sodré L., Stasińska G., Gomes J.M., 2005, *MNRAS*, 358, 363
- Conroy C., Graves G.J., van Dokkum P.G., 2014, *ApJ*, 780, 33
- Crawford S.M., et al., 2010, *Proceedings of the SPIE*, Volume 7737
- de Swardt B., Kraan-Korteweg R.C. & Jerjen H., 2010, *MNRAS*, 407, 955
- de Vaucouleurs G., et al. 1991 'Third reference catalogue of bright galaxies.', Springer (RC3)
- Falcón-Barroso J. et al. 2011, *A&A*, 532, 95
- Foster C., et al. 2012, *A&A*, 547, 79
- Gallazzi A., Charlot S., Brinchmann J., White S.D.M., 2006, *MNRAS*, 370, 1106
- Graves G.J., Schiavon R., 2008, *ApJS*, 177, 446
- Graves G.J., Faber S.M., Schiavon R.P., 2009, *ApJ*, 693, 486
- Grevesse N., Sauval A.J., 1998, *SSRv*, 85, 161
- Harrison C.D. et al., 2011, *MNRAS*, 413, 1036
- Izotov, Y.I., Thuan, T.X., & Lipovetsky, V.A., 1994, *ApJ*, 435, 647
- Izotov, Y.I. & Thuan, T.X. 1999, *ApJ*, 511, 639
- Izotov, Y.I., Stasińska, G., Meynet, G., Guseva, N.G., & Thuan, T.X., 2006, *A&A*, 448, 955
- Jerjen H., Binggeli B., Freeman K.C., 2000, *AJ*, 119, 593
- Karachentsev I.D., Kaisina E.I., 2013, *AJ*, 146, 46
- Kaviraj S., Rey S.-C., Rich R.M., Yoon S.-J., Yi S.K., 2007, *MNRAS*, 381, L74
- Kaviraj S., Devriendt J.E.G., Ferreras I., Yi S.K., Silk J., 2009, *A&A*, 503, 445
- Kelvin L.S. et al. 2014, *MNRAS*, 444, 1647
- Kniazev, A.Y., Pustilnik, S.A., Grebel, E.K., Lee, H., & Pramskij, A.G., 2004, *ApJS*, 153, 429
- Kniazev, A.Y., Grebel, E.K., Pustilnik, S.A., Pramskij, A.G., & Zucker, D., 2005, *AJ*, 130, 1558
- Kniazev, A.Y., Zijlstra, A.A., Grebel, E.K., et al. 2008, *MNRAS*, 388, 1667
- Koleva M., Bouchard A., Prugniel P., De Rijcke S., Vauglin I., 2013, *MNRAS*, 428, 2949
- Koleva M., Prugniel P., De Rijcke S., Zelinger W., 2011, *MNRAS*, 417, 1643
- Korn A.J., Maraston C., Thomas D., 2005, *A&A*, 438, 685
- Merlin E., et al., 2012, *MNRAS*, 427, 1530
- O'Donoghue D., et al. 2006, *MNRAS*, 372, 1510
- Pipino A., Devriendt J.E.G., Thomas D., Silk J., Kaviraj S., 2009, *A&A*, 505, 1075
- Recchi S., Calura F., Kroupa P., 2009, *A&A*, 499, 711
- Reines A.E., Nidever D.L., Whelan D.G., Johnson K.E., 2010, *ApJ*, 708, 26
- Rose J.A., et al. 1994, *AJ*, 108, 2054
- Sansom A.E., Northeast M.S., 2008, *MNRAS*, 387, 331
- Sansom A.E., Milone A.C., Vazdekis A., Sánchez-Blázquez P., 2013, *MNRAS*, 435, 952
- Saviane I., Ivanov V.D., Held E.V., Alloin D., Rich R.M., Bresolin F., Rizzi L., 2008, *A&A*, 487, 901
- Sarzi M., et al., 2006, *MNRAS*, 366, 1151
- Schiavon R.P., 2007, *ApJS*, 171, 146
- Schlegel, D., Finkbeiner, D., & Davis, M., 1998, *ApJ*, 500, 525
- Skillman E.D., et al., 1994, *ApJ*, 431, 172
- Skillman E.D., Côté S., Miller B.W., 2003, *AJ*, 125, 593
- Thomas D., Maraston C., Bender R., Mendes de Oliveira C., 2005, *ApJ*, 621, 673
- Tolstoy E., Hill V., Tosi M., 2009, *ARA&A*, Vol. 47, p371
- Vazdekis A., et al., 2010, *MNRAS*, 404, 1639
- Venn K.A., Irwin M., Shetrone M.D., Tout C.A., Hill V., Tolstoy E., 2004, *AJ*, 238 177
- Worthey G., Ottaviani D.L., 1997, *ApJS*, 111, 377
- Worthey G., 1998, *PASP*, 110, 888